

An Oscillating Langevin Antenna for Driving Plasma Turbulence Simulations

J. M. TenBarge

IREAP, University of Maryland, College Park, MD, USA

G. G. Howes

Department of Physics and Astronomy, University of Iowa, Iowa City, IA, USA

W. Dorland

IREAP, University of Maryland, College Park, MD, USA

G. W. Hammett

Princeton Plasma Physics Laboratory, Princeton, NJ, USA

Abstract

A unique method of driving Alfvénic turbulence via an oscillating Langevin antenna is presented. This method of driving is motivated by a desire to inject energy into a finite domain numerical simulation in a manner that models the nonlinear transfer of energy from fluctuations in the turbulent cascade at scales larger than the simulation domain. The oscillating Langevin antenna is shown to capture the essential features of the larger scale turbulence and efficiently couple to the plasma, generating steady-state turbulence within one characteristic turnaround time. The antenna is also sufficiently flexible to explore both strong and weak regimes of Alfvénic plasma turbulence.

Keywords: Numerical Methods; Langevin; Turbulence; Plasma

1. Introduction

The development of a detailed understanding of plasma turbulence is an outstanding goal of the plasma physics community due to its ubiquity and importance in a variety of environments. In space physics and astrophysics, turbulence mediates the transfer of energy from the large scales at which energy is injected into turbulent motions to the small scales at which the turbulent energy is ultimately dissipated as heat. The resulting heating of the plasma determines

Email address: jtenbarg@umd.edu (J. M. TenBarge)

the radiation emitted from turbulent astrophysical environments, which constitutes the majority of our observational data. In the heliosphere, turbulence likely plays a key role in the heating of the solar corona and in the launching of the solar wind. The dissipation of turbulent fluctuations in the streaming solar wind plasma impacts the overall thermodynamic balance of the heliosphere.

The near-Earth solar wind is a unique laboratory for the study of plasma turbulence due to its accessibility to direct spacecraft measurements. The Alfvénic nature of the turbulent fluctuations in the solar wind plasma has long been recognized [1, 2, 3]. Modern theories of anisotropic MHD turbulence suggest that the physical mechanism that drives the turbulent cascade of energy from large to small scales is the nonlinear interaction between counterpropagating Alfvén waves [4, 5, 6, 7, 8, 9, 10]. Although spacecraft missions enable detailed *in situ* measurements of many aspects of the turbulent plasma and electromagnetic fluctuations, measurements are generally possible at only a single point, or at most a few points, in space. The solar wind plasma typically streams past the spacecraft at super-Alfvénic velocities, so a time series of single-point measurements maps to the advection of spatial variations in the turbulent plasma [11]. These limitations of spacecraft measurements motivate complementary efforts to gain further insight into the nature of Alfvénic turbulence using terrestrial laboratory experiments or numerical simulations. Although the experimental measurement of the nonlinear interaction between counterpropagating Alfvén waves has recently been accomplished in the laboratory [12], the large length scales and low frequencies associated with Alfvénic fluctuations are particularly challenging to realize in the laboratory [13], and experiments thus far have been limited to the weak turbulence regime [12]. Numerical simulations of plasma turbulence, therefore, are indispensable tools to explore the fundamental nature of plasma turbulence, the mechanisms of its dissipation, and the resulting plasma heating.

The simulation of a turbulent plasma system typically requires the injection of energy into the turbulence at large scale and the dissipation of the turbulent energy at small scales. For many space and astrophysical plasma systems of interest, the dynamic range between the observed energy injection and dissipation scales exceeds current computational capabilities (a limit of approximately 3 orders of magnitude for 3D turbulence simulations). In addition, on the small scales at which the dissipation mechanisms serve to terminate the turbulent cascade of energy, the plasma dynamics is weakly collisional in many space and astrophysical plasmas of interest, so the dissipation is thought to be governed by some kinetic damping mechanism, such as collisionless wave-particle interactions [14, 15, 16]. Since it is not possible to include, in a single simulation with realistic physical parameters, both the large-scale process driving the turbulence and the kinetic physical dynamics governing the dissipation at small scales, a promising strategy is to focus on a sub-range of the complete turbulent cascade.

An exciting frontier in the study of plasma turbulence, one that has engendered vigorous recent activity [17, 18, 19, 20, 21], is the quest to identify the physical mechanisms that govern the dissipation of turbulence under weakly collisional conditions and to determine the resulting heating of the plasma species.

The sub-range of numerical simulations, in this case, begins with a domain scale that falls within the inertial range of the turbulent cascade and extends down to encompass the small, dissipative scales. Therefore, it is desirable to inject energy into the simulation at the domain scale in a manner that resembles the nonlinear transfer of energy, within the inertial range, from scales slightly larger than the simulation domain. In constructing such a technique for driving plasma turbulence simulations, it is essential to account for the inherent scale-dependent anisotropy of Alfvénic turbulence [7, 8, 9], which becomes more anisotropic as the turbulence cascades to smaller scales. Here we describe such a mechanism for forcing plasma turbulence simulations, the oscillating Langevin antenna, that models the Alfvénic fluctuations at the domain scale generated by the transfer of energy caused by nonlinear interactions between counterpropagating Alfvén waves at scales larger than the simulation domain. The method is effective in generating strong Alfvénic turbulence in kinetic simulations and flexible enough to simulate strong or weak turbulence.

The paper is organized as follows: In §2, we introduce some of the basic concepts underlying Alfvénic turbulence. §3 discusses the simple case of sinusoidal driving and plasma coupling before moving on to the more complicated oscillating Langevin antenna in §4. In the latter section, the antenna is described in detail and its domain of applicability is examined. The implementation of the antenna in AstroGK is explored and the amplitude necessary for driving strong turbulence is given in §5. §6 briefly discusses driving methods employed in other turbulence simulations. In §7, we present a summary of this paper.

2. Properties of Turbulence Relevant to Driving Mechanisms

A general picture of the turbulent energy spectrum in weakly collisional plasma turbulence is shown in Figure 1, where the values of the characteristic length scales are appropriate for the case of turbulence measured in the near-Earth solar wind [22, 1, 23, 14, 24, 25, 26, 27, 28, 29]. The transformation from the spacecraft-frame frequency of solar wind measurements to the perpendicular component of the wavevector k_{\perp} is accomplished by adopting Taylor’s hypothesis [11] and by assuming an anisotropy of the turbulent fluctuations, $k_{\parallel} \ll k_{\perp}$, as discussed below. Note that, unless otherwise stated, the energy discussed throughout will be the one-dimensional perpendicular magnetic energy as a function of perpendicular wavenumber, $E_{B_{\perp}}(k_{\perp}) = \int_{-\infty}^{\infty} dk_{\parallel} \int_0^{2\pi} d\theta k_{\perp} |\delta B_{\perp}(k_{\perp}, \theta, k_{\parallel})|^2 \simeq \delta B_{\perp}^2/k_{\perp}$, where perpendicular is normal to the local mean magnetic field and $\delta \mathbf{B}$ is the fluctuating magnetic field. The perpendicular wavenumber is normalized to the ion (proton) gyroradius, $\rho_i = v_{ti}/\Omega_i$, where $v_{ti} = \sqrt{2T_i/m_i}$ is the ion thermal velocity and $\Omega_i = eB_0/m_i c$ is the ion gyrofrequency.

At the largest scales ($k_{\perp} \rho_i < 10^{-4}$) in Figure 1, the timescale of nonlinear turbulent energy transfer exceeds the travel time from the sun [14, 30], so these large scale fluctuations have not yet evolved into a turbulent cascade. The turbulent fluctuations at these large scales, commonly denoted the *energy containing range*, are often assumed to be relatively isotropic with $k_{\parallel} \sim k_{\perp}$, and the energy spectrum is characterized by a spectral index of -1 .

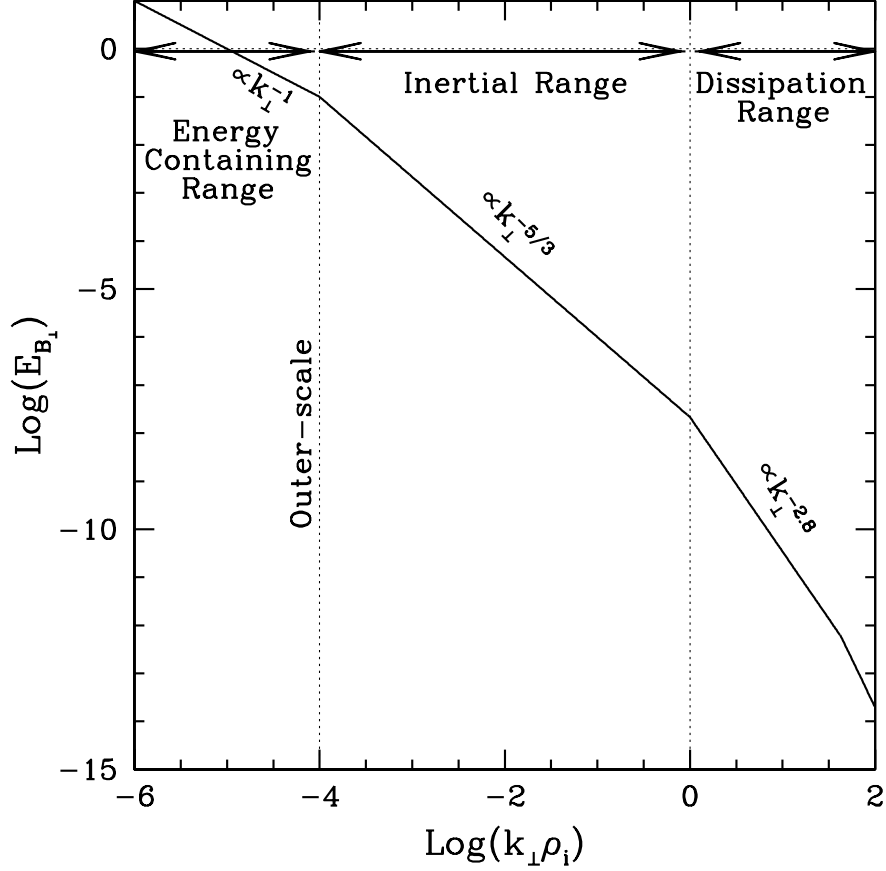


Figure 1: Schematic diagram of the turbulent evolution of energy from large to small scales.

At the outer scale of the turbulence inertial range ($k_{\perp}\rho_i \sim 10^{-4}$) in Figure 1, the timescale of the nonlinear energy transfer is approximately equal to the travel time of the solar wind plasma from the sun to 1 AU [14], so the turbulent cascade has just had time to develop at this scale, and the spectrum steepens to a spectral index of $-5/3$. The fluctuations at the outer scale are assumed to be isotropic, $k_{\parallel} \sim k_{\perp}$. The *inertial range* of the solar wind turbulent energy spectrum extends from the outer scale of the turbulence down to the scale of the ion gyroradius, $10^{-4} \lesssim k_{\perp}\rho_i \lesssim 1$. Within the inertial range, the energy transfer is believed to be dominated by local interactions in scale, leading to turbulent dynamics that are self-similar and independent of the driving and the dissipative microphysics [16]. Theoretical considerations suggest that the transfer of energy in Alfvénic turbulence is anisotropic, where energy is transferred more effectively to small perpendicular scales than to small parallel scales. The anisotropy of the

turbulence is scale-dependent, with $k_{\parallel} \propto k_{\perp}^q$, with predicted values of $q = 2/3$ [8] or $q = 1/2$ [9]. Support for these forms of spectral anisotropy have been observed extensively in the solar wind [31, 32, 33, 34, 28, 35, 36] and in numerical simulations [37, 38, 39, 40, 41, 42]. Regardless of which scaling is chosen for the anisotropy, at the end of the inertial range ($k_{\perp}\rho_i \sim 1$), the turbulent fluctuations are significantly anisotropic with $k_{\parallel} \ll k_{\perp}$.

The anisotropic turbulent cascade of Alfvén waves in the inertial range transitions to a cascade of kinetic Alfvén waves at the perpendicular scale of the ion gyroradius, $k_{\perp}\rho_i \sim 1$ [43, 14, 15, 24, 16, 28, 44, 45]. In the range below this scale ($k_{\perp}\rho_i \gtrsim 1$), often denoted the *dissipation range*, the energy spectrum steepens to a spectral index of approximately -2.8 , as measured in the solar wind [24, 25, 26, 27, 28, 29] and obtained in kinetic numerical simulations [46, 47]. The turbulent energy transfer is expected to become yet more anisotropic in this range, $k_{\parallel} \propto k_{\perp}^{1/3}$ [48, 14, 16], a prediction supported by electron MHD [48, 49] and kinetic numerical turbulence simulations [50]. Within this region, kinetic damping mechanisms, such as collisionless wave-particle interactions, can remove energy from the turbulent cascade, ultimately terminating the cascade and mediating the conversion of turbulent fluctuation energy to plasma heat.

Note that the scale-dependent anisotropy of the turbulent dynamics has important implications for the driving of turbulence simulations within the inertial range wherein $\delta B/B_0 \ll 1$ —the waves driven at the simulation domain scale must be anisotropic, at least with $k_{\parallel} < k_{\perp}$, and possibly with $k_{\parallel} \ll k_{\perp}$. It is an important, but often unappreciated, fact that using an isotropic driving mechanism to simulate a turbulent cascade starting within the inertial range is inconsistent with the known properties of plasma turbulence [40, 51, 52].

Given the current limitations of modern supercomputers, it is not possible to simulate self-consistently turbulence from the large driving scales and follow its evolution down to the smallest scales at which the turbulent cascade is terminated by some physical dissipation mechanism. For example, as depicted in Figure 1, the turbulent cascade begins at the outer scale $k_{\perp}\rho_i \sim 10^{-4}$, and continues through a transition at the scale of the ion gyroradius $k_{\perp}\rho_i \sim 1$ down to the scale of order the electron gyroradius at $k_{\perp}\rho_i \sim 10^2$. Modeling the turbulent cascade in three spatial dimensions over a dynamic range of 6 orders of magnitude while resolving the kinetic physics inherent to the dissipation mechanism is well beyond computing power for the foreseeable future. In light of this limitation, a number of different strategies have been adopted to realize progress on the computational front: (#1) simulating turbulence in reduced dimensionality, (#2) employing reduced dimensionless ratios of plasma parameters, or (#3) modeling turbulence only over a subrange of the turbulent cascade. We briefly discuss the limitations of each of these approaches, and then motivate the development of a physically realistic driving mechanism for the simulation of a subrange of the turbulent cascade.

Many recent efforts in the simulation of plasma turbulence have adopted strategy #1, to simulate the turbulent dynamics in reduced spatial dimensions [53, 17, 54, 55, 56, 19, 57, 21]. The nature of Alfvénic turbulence, however,

is inherently three-dimensional, with variation in the direction parallel to the magnetic field required to describe the physics of Alfvén waves, and with variation in both dimensions perpendicular to the magnetic field required to capture the dominant nonlinear term [46]. Therefore, any two-dimensional description incompletely describes the physical effects that play a role in Alfvénic plasma turbulence.

Strategy #2 is to employ reduced ratios of plasma parameters to enable a computationally feasible calculation. For example, for a fully ionized hydrogenic plasma of protons and electrons with equal temperatures $T_i/T_e = 1$, the ratio of the ion to electron gyroradius ρ_i/ρ_e is equal to the square root of the mass ratio m_i/m_e , which has a physical value $m_i/m_e = 1836$. Therefore, the ratio of gyroradii is $\rho_i/\rho_e = \sqrt{m_i/m_e} \simeq 43$. Reducing the mass ratio to $m_i/m_e = 100$ preserves the limit $m_i/m_e \gg 1$ but reduces the ratio of gyroradii to $\rho_i/\rho_e = 10$, lowering the computational resolution required to cover the range of scales from the ion to the electron gyroradius. The primary disadvantage of using dimensionless ratios that are reduced from their physical values is that the numerical results often cannot be directly compared with observational or experimental measurements. In addition, reducing the extent of a finite dynamic range, as in the reduction of ρ_i/ρ_e from 43 to 10, may lead to not only quantitative, but possibly also qualitative, changes in the results. Continuing the example above of using a reduced mass ratio to reduce the scale separation between ρ_e and ρ_i , since collisionless Landau damping by ions peaks at $k_\perp \rho_i \sim 1$ and by electrons peaks at $k_\perp \rho_e \sim 1$, reduction of the mass ratio can artificially enhance electron damping at the ion scale, qualitatively changing the amount of dissipated energy absorbed by electrons, and likely altering the scaling of the magnetic energy spectrum in the dissipation range, since the spectrum is determined by a balance of the rate of nonlinear energy transfer to the rate of collisionless damping [14, 46].

The viewpoint of the authors is that strategy #3, to model the turbulence only over a subrange of the turbulent cascade, can achieve a computationally feasible calculation without sacrificing the advantage of physical realism. Since a steady-state turbulent spectrum can only be achieved by a steady rate of energy injection into the turbulence at large scales and an equal rate of resolved turbulent energy dissipation at small scales, this problem reduces to constructing appropriate numerical mechanisms for turbulent driving and dissipation. Turbulence simulations that directly model the driving scale of the turbulence require some numerical dissipation mechanism to remove energy from the simulation at the smallest resolved scales (where the scale corresponding to the physical dissipation mechanism is unresolved¹). Similarly, simulations that aim

¹Historically, simulations of MHD turbulence have followed this strategy, modeling the driving of the turbulence at the outer scale and using viscosity and resistivity as the dissipation mechanism. Viscosity and resistivity are fluid closures for the dissipation in the strongly collisional limit, a limit not applicable to the weakly collisional conditions of many space, astrophysical, and laboratory plasmas of interest. Therefore, viscosity and resistivity in MHD turbulence simulations often represent *ad hoc* numerical mechanisms for dissipation, generally

to model directly the physical dissipation mechanisms require some numerical mechanism for injecting energy into the turbulence at the domain scale (where the scale corresponding to the physical driving mechanism is larger than the simulation domain). It is also possible to model the central range of the turbulent cascade (for example, to model the transition at $k_{\perp}\rho_i \sim 1$ in Figure 1), where both a numerical driving mechanism and a numerical dissipation mechanism are required [43]. *The focus of this paper is to describe a physically motivated mechanism for numerical driving of plasma turbulence simulations where the simulation domain is smaller than the physical driving scale of the turbulent cascade. The key physical concept motivating our implementation of the driving is that the turbulent cascade is mediated by nonlinear interactions between counterpropagating Alfvén waves. We find that this manner of driving minimizes the transition from the driving scale to the inertial regime of the turbulence, thereby maximizing the effective dynamic range of the turbulent cascade.*

The effort to devise an appropriate numerical mechanism for driving turbulence to simulate the small-scale end of the turbulent cascade is motivated by the intense interest that has recently arisen in identifying and characterizing the physical processes responsible for the dissipation of plasma turbulence and the consequent heating of the plasma species. Vigorous efforts to address this new frontier in plasma turbulence have been driven by significant advances in observational studies, enabling direct measurements of the turbulence at the dissipative scales in the near-Earth solar wind [24, 25, 26, 27, 28, 29], and in numerical methods for study of kinetic dissipation mechanisms [43, 58, 17, 59, 60, 61, 53, 46, 62, 50, 63, 19, 20, 21].

The anisotropy inherent in magnetized plasma turbulence introduces subtle, but important, complications in devising an appropriate mechanism for turbulent energy injection into a simulation domain whose largest scale falls within the inertial range. The characteristic anisotropy in wavevector space over different scale ranges of Alfvénic plasma turbulence, as described earlier in this section, is depicted in Figure 2. At the outer scale $k_{\perp}\rho_i \sim 10^{-4}$, the turbulent fluctuations are believed to be approximately isotropic, with $k_{\parallel} \sim k_{\perp}$. But energy is transferred through the inertial range preferentially to smaller perpendicular scales, as described by the scale-dependent anisotropy, $k_{\parallel} \propto k_{\perp}^q$, where we have adopted the Goldreich-Sridhar model for turbulence with $q = 2/3$ [8] to construct this figure. When the turbulent cascade enters the dissipation range at $k_{\perp}\rho_i \sim 1$, the turbulence becomes yet more anisotropic, with a scaling $k_{\parallel} \propto k_{\perp}^{1/3}$ [48, 14, 16, 50]. Turbulent power is believed to fill the region below this boundary of critical balance, filling the shaded region in the figure [8, 38, 14, 50]. A simulation intended to model the central part of the turbulent cascade, as depicted in Figure 2, must take into account the characteristic anisotropy of the turbulent fluctuations in three important ways. First, the simulation domain must reflect the anisotropy of the turbulence, which motivates using an elon-

not rigorous models of the physical mechanisms responsible for the dissipation of turbulence in a weakly collisional plasma.

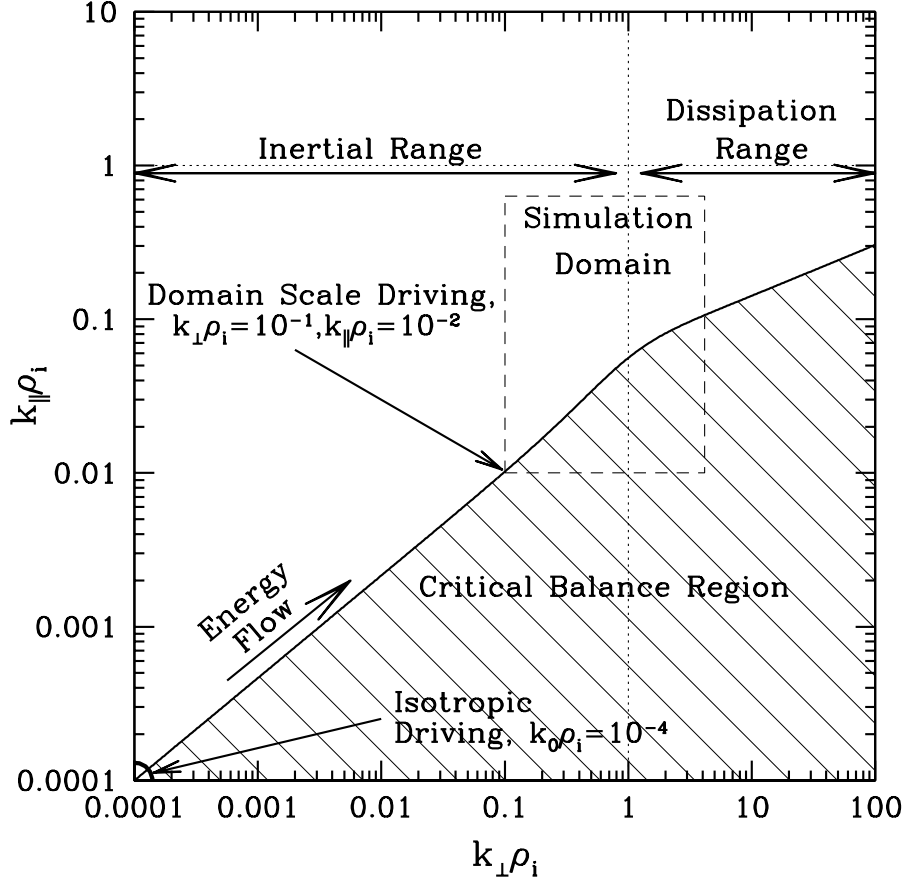


Figure 2: Schematic diagram of the distribution of energy in the $k_{\perp} - k_{\parallel}$ plane, highlighting the turbulence driving scale, typical simulation domain, and domain scale driving.

gated domain to describe optimally the turbulent fluctuations. And, second, the numerical mechanism for driving the turbulence must drive fluctuations with the expected anisotropy of the turbulence at the domain scale. The third and final consideration, if the simulation is intended to model the case of strong turbulence [7, 8], is that the amplitude of the turbulent driving should generate turbulent fluctuations satisfying the condition of critical balance [64, 8]. These three aspects of simulating turbulence have been implemented by a number of other authors, e.g., [38, 51, 65, 52].

The wavenumber range in $(k_{\perp}, k_{\parallel})$ that is covered by a modest simulation of a subrange of the physical turbulent cascade is depicted in Figure 2 by the dashed box. Note that, in $(k_{\perp}, k_{\parallel})$ space, the lower left corner of this dashed box corresponds to the perpendicular and parallel domain scale, and the upper right corner corresponds to the perpendicular and parallel resolution. In the

case plotted in Figure 2, the simulation domain scale is given by $(k_{\perp 0}\rho_i, k_{\parallel 0}\rho_i) = (10^{-1}, 10^{-2})$, so that the simulation domain is an elongated box of dimensions $L_{\parallel 0} \times L_{\perp 0}^2$, where $L_{\parallel 0} = 200\pi\rho_i$ and $L_{\perp 0} = 20\pi\rho_i$. Similarly, the fully de-aliased resolution of the simulation is $\Delta l_{\parallel} \simeq 4.5\pi\rho_i$ and $\Delta l_{\perp} \simeq \pi\rho_i/2$. The elongation of the simulation domain is chosen so that the largest scale perpendicular and parallel fluctuations correspond to the anisotropic fluctuations that coincide with the condition of critical balance (the line along the upper boundary of the shaded region in Figure 2). By driving the anisotropic turbulent fluctuations at the domain scale (in which $k_{\perp 0} > k_{\parallel 0}$) at the amplitude specified for critical balance, a cascade of strong plasma turbulence can be driven. This numerical mechanism for driving the turbulence is inspired by the physical properties of Alfvénic turbulence.

Modern theories of anisotropic incompressible MHD turbulence are based on the key concept that the turbulent cascade of energy from large to small scales is driven by the nonlinear interaction between counterpropagating Alfvén waves [5, 7, 8, 9, 12]. Therefore, our numerical mechanism for driving the turbulence in a physically realistic manner is to drive Alfvén waves that travel both up and down the equilibrium magnetic field. Since the Alfvén wave in the MHD limit, $k\rho_i \ll 1$, has no parallel magnetic field perturbation, $\delta B_{\parallel} = 0$, an Alfvén wave can be driven effectively by applying a parallel current throughout the simulation domain (corresponding to generating a body force). The parallel current is applied across the domain as a plane wave with the wavevector and frequency of the desired Alfvén wave. If the driven waves reach amplitudes satisfying the condition of critical balance, nonlinear interactions between these driven Alfvén waves rapidly generate a turbulent cascade of energy to small scales. The condition of critical balance implies that the timescale of the nonlinear energy transfer balances the linear timescale of the interacting Alfvén waves, thus the frequency of the plane wave component of parallel current is chosen to be approximately the linear frequency of the domain scale Alfvén waves, and the driving should decorrelate on approximately the same timescale. The aim of this numerical driving method is to model the nonlinear transfer of energy from counterpropagating Alfvén waves at scales larger than the simulation domain to the domain scale Alfvén waves. This physically motivated driving is accomplished with the *Oscillating Langevin Antenna*, defined and characterized in the remainder of this paper.

3. A Simple Model of Antenna Driving

Before discussing the complexities of an antenna driven by a Langevin equation, we begin by discussing the simple case of sinusoidal driving of an incompressible MHD plasma to understand the general response of the plasma as a function of driving frequency. The incompressible MHD equations can be cast in Elsasser form [66] as

$$\frac{\partial \mathbf{z}^{\pm}}{\partial t} \mp \mathbf{v}_A \cdot \nabla \mathbf{z}^{\pm} = -\mathbf{z}^{\mp} \cdot \nabla \mathbf{z}^{\pm} - \nabla P / \rho_0 + \nu \nabla^2 \mathbf{z}^{\pm} + \mathbf{F}^{\pm}, \quad (1)$$

$$\nabla \cdot \mathbf{z}^\pm = 0, \quad (2)$$

where the magnetic field is decomposed into equilibrium and fluctuating parts $\mathbf{B} = \mathbf{B}_0 + \delta\mathbf{B}$, $\mathbf{v}_A = \mathbf{B}_0/\sqrt{\mu_0\rho_0}$ is the Alfvén velocity due to the equilibrium field $\mathbf{B}_0 = B_0\hat{\mathbf{z}}$, P is total pressure (thermal plus magnetic), ρ_0 is mass density, the Laplacian term leads to damping where viscosity and resistivity have been set equal $\nu = \eta$, \mathbf{F}^\pm is an external forcing, and $\mathbf{z}^\pm = \mathbf{u} \pm \delta\mathbf{B}/\sqrt{4\pi\rho_0}$ are the Elsässer fields given by the sum and difference of the velocity fluctuation \mathbf{u} and the magnetic field fluctuation $\delta\mathbf{B}$ expressed in velocity units. The divergence condition (2) specifies the pressure in the incompressible plasma [10],

$$\nabla^2 P/\rho_0 = -\nabla \cdot (\mathbf{z}^\mp \cdot \nabla \mathbf{z}^\pm). \quad (3)$$

The second term on the left-hand side of (1) is the linear term representing the propagation of the Elsässer fields along the mean magnetic field at the Alfvén speed, the first term on the right-hand side is the nonlinear term representing the interaction between counterpropagating waves, and the second term on the right-hand side is a nonlinear term that enforces incompressibility through (3).

Focusing on the evolution of a single Fourier mode \mathbf{z}_k^\pm , we choose to write (1) in the simplified functional form

$$\frac{\partial \mathbf{z}_k^\pm}{\partial t} \mp i\omega_l \mathbf{z}_k^\pm + \gamma \mathbf{z}_k^\pm = \mathbf{F}_k^\pm, \quad (4)$$

where the second term on the left-hand side represents the characteristic linear response where the linear frequency is $\omega_l = k_\parallel v_A$, and the third-term represents the loss of energy from the single Fourier mode \mathbf{z}_k^\pm with effective frequency γ . Here, the loss term $\gamma = \omega_{nl} + \nu k^2$ combines two separate physical effects: (i) linear damping due to viscosity and resistivity given by νk^2 ; and (ii) the nonlinear transfer of energy through interactions with all other Fourier modes via the nonlinear interaction and pressure terms, where we generalize the effects of these terms as a nonlinear frequency response, $\omega_{nl} \mathbf{z}_k^\pm \sim \mathbf{z}^\mp \cdot \nabla \mathbf{z}_k^\pm + \nabla P/\rho_0$.

The physics described by (4) is similar to the physics of the driven, damped harmonic oscillator, described by

$$\frac{d^2 x}{dt^2} + \gamma \frac{dx}{dt} + \omega_l^2 x = F. \quad (5)$$

If F is assumed to be a sinusoidal driving of the form $F = A_0 \sin \omega t$, then the steady-state portion of the solution to (5) is

$$x(t) = \frac{A_0}{\sqrt{(\omega_l^2 - \omega^2)^2 + \gamma^2 \omega^2}} \sin(\omega t + \delta), \quad (6)$$

where $\delta = \arctan[-\omega\gamma/(\omega_l^2 - \omega^2)]$. Solving (4) via a similar Fourier transform method yields a steady-state amplitude response of

$$|\mathbf{z}_k^\pm| = \frac{A_0}{\sqrt{(\omega_l - \omega)^2 + \gamma^2}}. \quad (7)$$

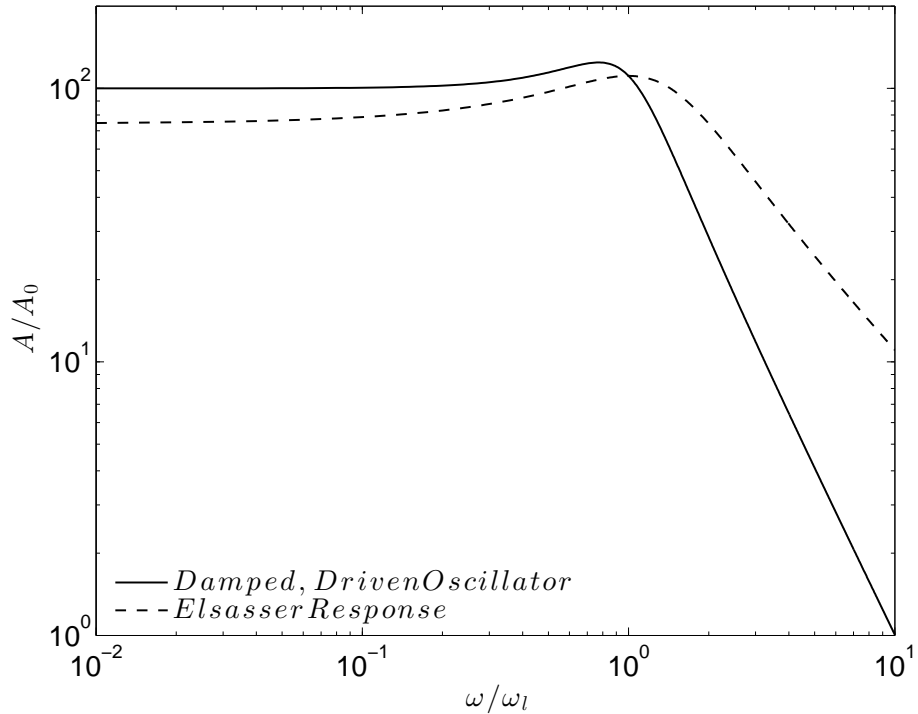


Figure 3: The normalized amplitude A/A_0 vs. normalized driving frequency ω/ω_l for a driven, damped harmonic oscillator (solid) and for (4) describing an incompressible MHD plasma (dashed) with $\gamma/\omega_l = 0.9$.

Although the mathematical forms of these solutions to (4) and (5) are not identical, they do share a similar qualitative form, demonstrating that the solution for a single Fourier mode in a sinusoidally driven incompressible MHD plasma will share similar physical properties with the driven, damped harmonic oscillator.

We now consider the response of a single Fourier mode in Alfvénic turbulence according to (4). The condition of critical balance in the case of strong MHD turbulence implies a balance between the linear and nonlinear frequencies $\omega_{nl} \sim \omega_l$ [8, 14, 46]. In addition, we are interested in the regime where the linear damping rate is weak, $\nu \ll \omega_l$. Consequently, we expect the energy loss rate for a single Fourier mode in strong Alfvénic turbulence to be represented by $\gamma \sim \omega_l$.

For sinusoidal driving of the form $A_0 \sin \omega t$, we plot the normalized amplitude response A/A_0 as a function of the normalized driving frequency ω/ω_l for both the case of the driven, damped harmonic oscillator (solid) and the case of the solution to Elsasser equation (4) for an incompressible MHD plasma (dashed) in Figure 3. In this plot, we have taken the energy loss rate, dominated by nonlinear energy transfer in the case of the turbulent plasma, as $\gamma/\omega_l = 0.9$. Defining the resonant frequency ω_R as the driving frequency resulting in the maximum

amplitude response, for the case of the driven, damped harmonic oscillator, we obtain $\omega_R/\omega_l = \sqrt{1 - (1/2)(\gamma/\omega_l)^2}$; for the case of the incompressible MHD plasma, we obtain $\omega_R/\omega_l = 1$. For driving frequencies below the resonant frequency, $\omega < \omega_R$, the resulting amplitude is essentially constant. For frequencies above resonance, however, the coupling becomes very poor, due to the injection and removal of energy faster than the oscillator or plasma can respond.

Using the intuition gained from this exploration of the linear response of a given mode, we address the issue of how to choose an appropriate driving frequency for simulations of plasma turbulence. In order to obtain efficient coupling between the driving antenna and the plasma, the analysis above demonstrates that one must drive with a frequency at or below the resonant frequency, which is approximately equal to the linear frequency. Therefore, we choose a driving frequency $\omega \lesssim \omega_l$. If one attempts to drive the plasma with a frequency above the linear frequency of the wavenumber mode being excited, there will be an impedance mismatch and very little energy will enter the plasma, analogous to the case of a damped, driven harmonic oscillator. This effect has been observed by Parashar et al. [67] in 2D hybrid kinetic numerical simulations. For the case of strong turbulence, the nonlinear energy transfer frequency balances the linear frequency, $\omega_{nl} \sim \omega_l$ [8, 14, 46]. Since our antenna aims to model the nonlinear energy transfer from fluctuations at slightly larger scales than our simulation volume, we expect the driving frequency to be given by the nonlinear frequency, $\omega \sim \omega_{nl}$. Therefore, for realistic driving of turbulence simulations at a driving scale within the turbulent inertial range, the appropriate choice is a driving frequency that is the same order of magnitude as the linear frequency, $\omega \sim \omega_l$, which fortunately ensures good coupling of the antenna to the turbulent plasma.

4. Oscillating Langevin Antenna

4.1. Numerical Implementation of Antenna

We wish to construct an antenna that will drive Alfvénic fluctuations in a simulation of plasma turbulence. For a plasma with an equilibrium magnetic field, $\mathbf{B}_0 = B_0 \hat{\mathbf{z}}$, the eigenfunction for the Alfvén wave has no magnetic field fluctuation in the direction parallel to the equilibrium magnetic field, $\delta B_z = 0$. Maxwell’s equations require that $\nabla \cdot \mathbf{B} = 0$, which reduces to $\mathbf{k}_\perp \cdot \delta \mathbf{B}_\perp = 0$ for a plane Alfvén wave with wavevector $\mathbf{k} = \mathbf{k}_\perp + k_z \hat{\mathbf{z}}$. To drive a general perpendicular magnetic field fluctuation $\delta \mathbf{B}_\perp$, one can impose through the plasma a current parallel to the equilibrium magnetic field, $\mathbf{J} = J_z \hat{\mathbf{z}}$. Since we can express the magnetic field fluctuation in terms of the curl of a vector potential, $\delta \mathbf{B} = \nabla \times \mathbf{A}$ and the current in terms of the curl of the magnetic field, $\mathbf{J} = (c/4\pi) \nabla \times \mathbf{B}$, a parallel current can be generated by driving the parallel component of the vector potential according to $J_z = -(c/4\pi) \nabla^2 A_z$. The magnetic field generated by this parallel vector potential is given by

$$\delta \mathbf{B}_\perp = -\hat{\mathbf{z}} \times \nabla A_z = i(k_y A_z \hat{\mathbf{x}} - k_x A_z \hat{\mathbf{y}}). \quad (8)$$

Therefore, a given Fourier mode of $\delta \mathbf{B}_\perp$ can be generated by specifying a Fourier mode of A_z with wavevector $\mathbf{k} = k_x \hat{\mathbf{x}} + k_y \hat{\mathbf{y}} + k_z \hat{\mathbf{z}}$.

Our implementation of the *oscillating Langevin antenna* drives a parallel body current through the plasma, where the properties of the antenna are specified by four parameters:

1. Wave vector \mathbf{k}
2. Amplitude A_0
3. Characteristic frequency ω_0 (real)
4. Decorrelation rate $\gamma_0 < 0$ (real).

Note that the frequency and decorrelation rate can be written together more concisely in complex notation as $\omega_a = \omega_0 + i\gamma_0$. The parallel vector potential of the antenna A_{za} is given by

$$A_{za}(k_x, k_y, k_z, t) = a_n e^{i\mathbf{k}\cdot\mathbf{r}}, \quad (9)$$

where the discrete (complex) value of the driving coefficient at timestep n is $a_n = a(t_n)$. We initialize the driving coefficient as $a_0 = A_0 \exp(i\phi)$, where the choice of phase, ϕ , is arbitrary.

The driving coefficient is evolved by the equation

$$a_{n+1} = a_n e^{-i\omega_a \Delta t} + F_a \Delta t, \quad (10)$$

where

$$F_a = \sigma u_n, \quad (11)$$

u_n is a delta-correlated uniform complex random number, $Re(u_n) \in [-1/2, 1/2]$ and $Im(u_n) \in [-1/2, 1/2]$, σ is an amplitude to be determined by the requirement that the antenna amplitude satisfy $\langle |a_n|^2 \rangle = A_0^2$, and brackets indicate an ensemble average. Applying this requirement to equation (10) leads to

$$A_0^2 (1 - e^{2\gamma_0 \Delta t}) = \sigma^2 \Delta t^2 \langle |u_n|^2 \rangle. \quad (12)$$

For numerical convergence, we require that $|\omega_a| \Delta t \ll 1$. Also, $\langle |u_n|^2 \rangle = 1/6$ for u_n as defined above. Therefore,

$$\sigma = A_0 \sqrt{12 \frac{|\gamma_0|}{\Delta t}}. \quad (13)$$

Note that this definition of σ is only valid for u_n as defined above. For instance, u_n constructed from a Gaussian complex random number would result in a different value for σ .

The relation between (10) and a standard stochastic process becomes more apparent when converted to the form of a finite difference advance in time using $e^{-i\omega_a \Delta t} \simeq 1 - i\omega_a \Delta t$ to yield

$$\frac{a_{n+1} - a_n}{\Delta t} = -i\omega_a a_n + F_a. \quad (14)$$

The continuous version of this equation is thus

$$\frac{da}{dt} = -i\omega_0 a + \gamma_0 a + F_a. \quad (15)$$

If we take $a = dv/dt$, then Fourier transforming in time yields $a = -i\omega_0 v$. Substituting this relation into (15) shows that this is the equation of a stochastically driven and damped harmonic oscillator [68]

$$\frac{da}{dt} = -\omega_0^2 v + \gamma_0 a + F_a. \quad (16)$$

Physically, (16) describes the motion of a harmonic oscillator with characteristic frequency ω_0 and damping rate γ_0 , where damping is due to stochastic particle collisions which serve to both damp the oscillator and cause random fluctuations. In the absence of the oscillating term in (16), it reduces to the standard Langevin equation describing Brownian motion [69]. Although our antenna is not governed by particle collisions, it obeys (16); therefore, we refer to our antenna as an *oscillating Langevin antenna*.

An important note should be made here: Although our driving method includes a Gaussian random number, u_n , which represents white noise, (10) integrates the white noise to achieve Brownian motion. White noise, depicted in Figure 10, applies energy equally at all frequencies, while the oscillating Langevin antenna applies energy with a peak centered on the driving frequency.

Fourier transforming (15) yields a squared amplitude response of the antenna in the form of a Lorentzian peaked about the antenna driving frequency

$$|a|^2 = \frac{\sigma^2 |\tilde{u}_n|^2}{(\omega - \omega_0)^2 + \gamma_0^2}, \quad (17)$$

where \tilde{u}_n is the Fourier transform of u_n (white noise). As expected, the full-width at half-maximum (FWHM) of the antenna amplitude is proportional to the decorrelation rate, $\text{FWHM} = 2\sqrt{3}\gamma_0$.

4.2. Examples of Driving by Oscillating Langevin Antenna

In Figure 4, we present an example of the evolution and frequency response of the oscillating Langevin antenna with amplitude $A_0 = 100$, angular frequency $\omega_0 = 2\pi$ rad/s, and decorrelation rate $\gamma_0 = -1$ rad/s. Note that this driving angular frequency corresponds to a *linear* frequency $f = 1$ Hz. The figure was produced by evolving equation (10) for 128 periods with $\Delta t = 2\pi/(\omega_0 n_p) = 1/64$ s, where $n_p = 64$ is the number of points per period. The Nyquist frequency is thus $\omega_{Nq} = 2\pi/2\Delta t = \omega_0 n_p/2 = 64\pi$ rad/s. In the upper panel, the real (blue), imaginary (red), and amplitude (green) of the antenna are plotted over only the first ten periods. In the second panel, the amplitude (green), the amplitude with a boxcar average with width 250 points applied (red), and the average amplitude (black) are plotted for the full 128 periods. In the third panel, the Fourier transform of the antenna (green) and a boxcar averaged

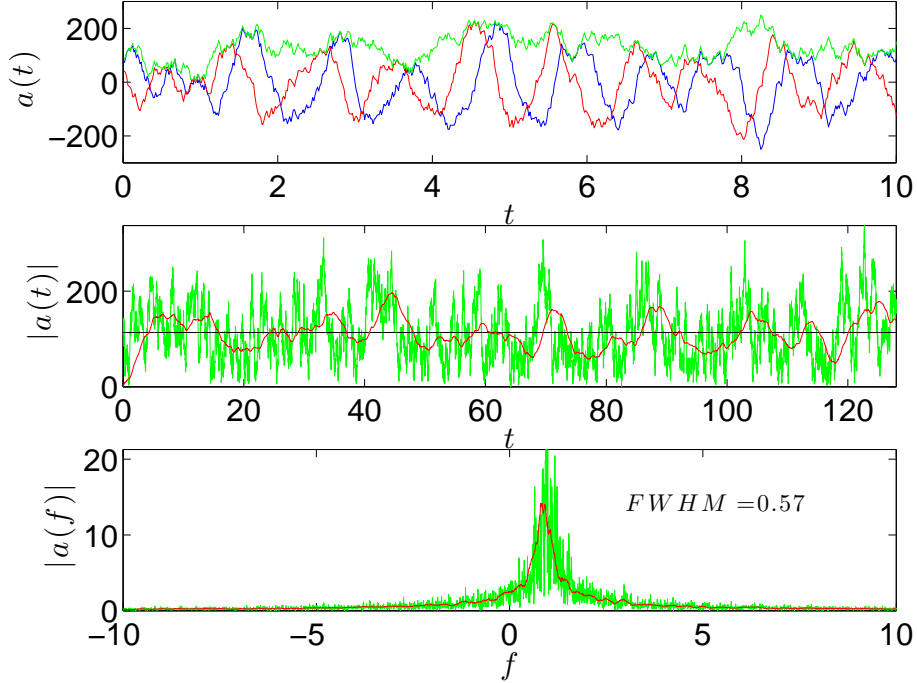


Figure 4: Temporal evolution of a single oscillating Langevin antenna with $A_0 = 100$, $\omega_0 = 2\pi$ rad/s, and $\gamma_0 = -1$ rad/s. Top: Real (blue), imaginary (red), and the magnitude (green) of the complex vector potential over 10 periods. Middle: Magnitude (green), boxcar average of the magnitude (red), and overall average of the magnitude (black) of a over 128 periods. Bottom: The frequency spectrum of the antenna (green) and its boxcar average (red) along with the full-width at half-maximum.

(width of 25 points) version of the amplitude (red) of the full 128 periods are plotted. Performing an average of 64 ensembles, we obtain an average amplitude $\langle |a| \rangle = 103 \pm 54$, average linear frequency $\langle f \rangle = 1.003 \pm 0.083$ Hz, and average $\langle \text{FWHM} \rangle = 0.57 \pm 0.08$ Hz, where brackets indicate ensemble averages and errors represent one standard deviation. The theoretical FWHM based on the Lorentzian response is $\text{FWHM} = 0.55$ Hz. The ensemble averages and the temporal response of the antenna represent excellent agreement with the values specified for the driving.

A similar single simulation with parameters $A_0 = 100$, $\omega_0 = 2\pi$ rad/s, $\gamma_0 = -2\pi$ rad/s, and $n_p = 64$ is presented in Figure 5. Again, performing an average of 64 ensembles, we find $\langle |a| \rangle = 107 \pm 55$, $\langle f \rangle = 0.97 \pm 0.32$ Hz, and $\langle \text{FWHM} \rangle = 3.1 \pm 0.3$ Hz. The theoretical FWHM based on the Lorentzian response is $\text{FWHM} = 3.4$ Hz. As expected for this case, the amplitude and central frequency are statistically unchanged from the first simulation, but the decorrelation rate (quantized by the FWHM) is larger, indicating the energy of the antenna will be spread into a wider range of frequencies than the first case.

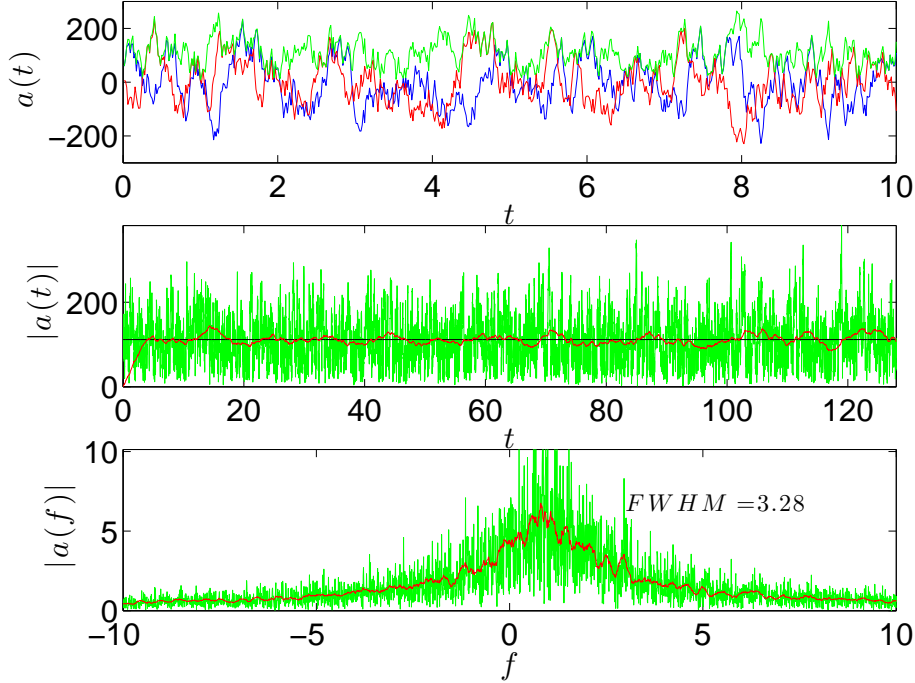


Figure 5: Temporal evolution of a single oscillating Langevin antenna with $A_0 = 100$, $\omega_0 = 2\pi$ rad/s, and $\gamma_0 = -2\pi$ rad/s. Top: Real (blue), imaginary (red), and the magnitude (green) of the complex vector potential over 10 periods. Middle: Magnitude (green), boxcar average of the magnitude (red), and overall average of the magnitude (black) of a over 128 periods. Bottom: The frequency spectrum of the antenna (green) and its boxcar average (red) along with the full-width at half-maximum.

4.3. Characterization of Antenna Behavior

The effective independent dimensionless variables determining the antenna evolution for a given amplitude A_0 and driving frequency ω_0 are the normalized decorrelation rate γ_0/ω_0 and normalized time step $\omega_0\Delta t$. To explore the region of validity of the antenna, we choose fiducial values corresponding to the second set of parameters presented above, $A_0 = 100$, $\omega_0 = 2\pi$ rad/s, $\gamma_0 = -2\pi$ rad/s, and $\omega_0\Delta t = 2\pi/n_p = \pi/32$ and separately vary γ_0 and Δt to characterize the behavior of the antenna in terms of the resulting average amplitude, FWHM, and frequency.

The results of varying the decorrelation rate γ_0 are presented in Figure 6. The circles correspond to ensemble averages over 64 ensembles, error bars are the standard deviation, and dotted lines correspond to the expected theoretical values. Although the FWHM is well-behaved for all values of γ_0 , the average amplitude and central frequency begin to deviate significantly from their theoretical values for $\gamma_0/\omega_0 \gtrsim 4$.

The effect of variation in the time step size Δt is presented in Figure 7. Again, we see that the antenna is well behaved for $\omega_0\Delta t \lesssim 0.4$. This behavior

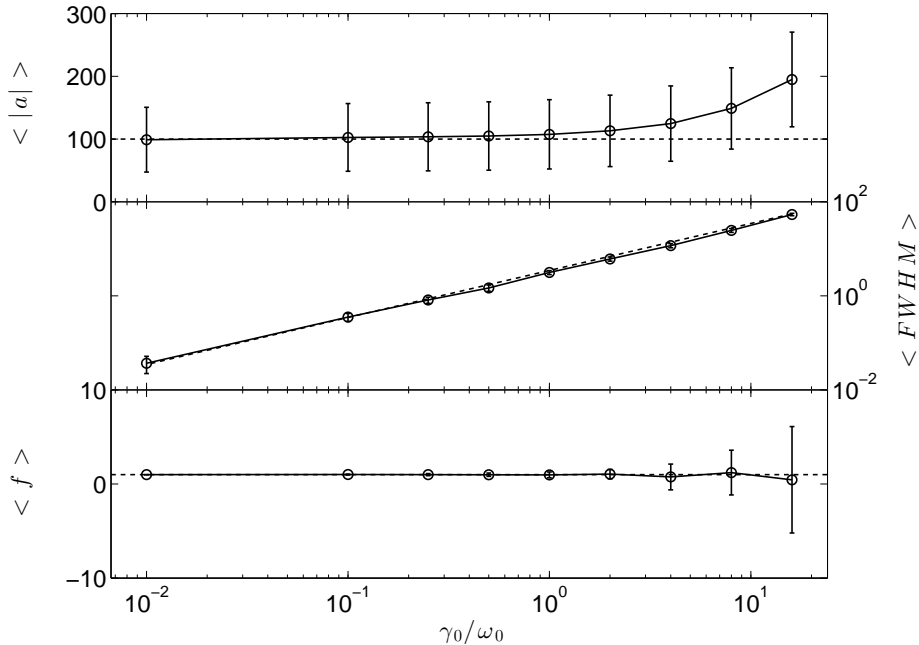


Figure 6: The average amplitude, FWHM, and central frequency of the oscillating Langevin antenna over 64 identically prepared ensembles with $A_0 = 100$, $\omega_0 = 2\pi$ rad/s, and $\omega_0\Delta t = \pi/32$ fixed as the decorrelation rate, γ_0 , is varied. The circles and error bars represent the ensemble average and standard deviation, and the dotted lines represent the theoretical values.

is expected because we assumed $|\omega_a|\Delta t \ll 1$ in the derivation of the discrete form of the Langevin equation. Note, the very poor agreement for the FWHM at $\omega_0\Delta t = \pi/2$ is due to the FWHM extending beyond the Nyquist frequency for this case.

The results above demonstrate quantitatively that the antenna is well behaved for sufficiently small time steps and decorrelation rates. As discussed in the following section, the decorrelation rates of interest for plasma turbulence simulations are $\gamma_0/\omega_0 \lesssim 1$, within the regime of acceptable behavior. Similarly, numerical convergence of simulation results always requires sufficiently small time steps satisfying $\omega_0\Delta t \ll 1$. Therefore, our implementation of the oscillating Langevin antenna is expected to be well behaved for the proposed use of driving plasma turbulence simulations.

5. Implementation

Having defined and characterized the oscillating Langevin antenna in Section 4, we now describe the use of the antenna for driving plasma turbulence simulations in the Astrophysical Gyrokinetics Code, AstroGK.

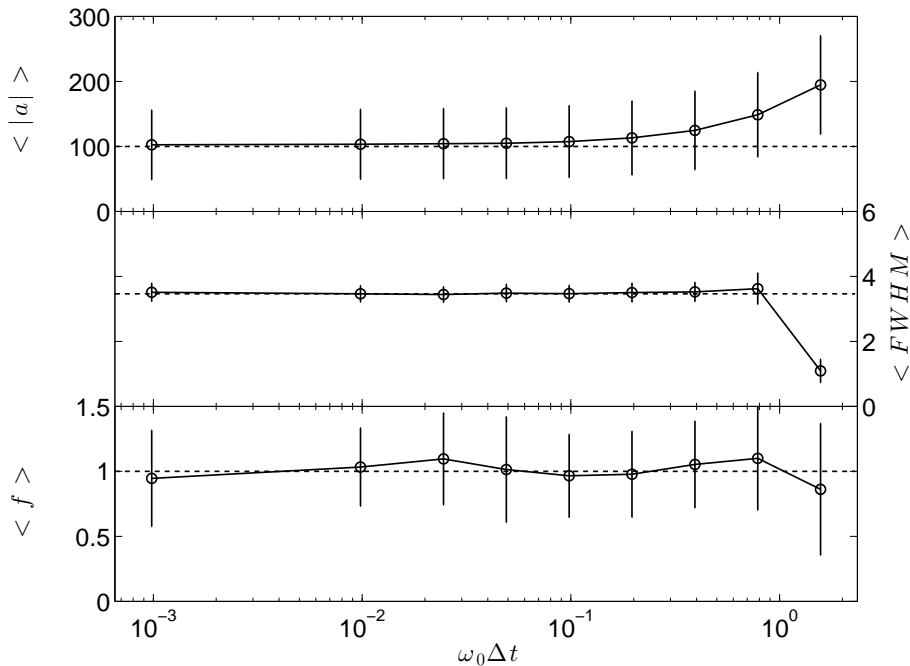


Figure 7: The average amplitude, FWHM, and central frequency of the oscillating Langevin antenna over 64 identically prepared ensembles with $A_0 = 100$ and $\omega_0 = -\gamma_0 = 2\pi$ rad/s fixed as the time step, Δt , is varied. The circles and error bars represent the ensemble average and standard deviation, and the dotted lines represent the theoretical values.

5.1. AstroGK

A detailed description of AstroGK and the results of linear and nonlinear benchmarks are presented in [59], so we only provide here a brief overview of the code.

AstroGK is an Eulerian slab code with triply periodic boundary conditions that solves the electromagnetic gyroaveraged Vlasov-Maxwell five-dimensional system of equations. It solves the gyrokinetic equation and gyroaveraged Maxwell's equations for the perturbed gyroaveraged distribution function, $h_s(x, y, z, \lambda, \epsilon)$, for each species s , the parallel gyroaveraged potential A_z , the parallel magnetic field perturbation δB_z , and the scalar potential ϕ [70, 71]. The simulation domain is elongated in the direction of the equilibrium magnetic field. Velocity space coordinates are related to the energy, $\epsilon = v^2/2$, and pitch angle, $\lambda = v_{\perp}^2/v^2$. The equilibrium velocity distribution for all species is treated as Maxwellian, and a realistic mass ratio, $m_p/m_e = 1836$, is employed for all simulations. The x - y plane is treated pseudospectrally, and an unwinded finite-differencing approach is employed for the z -direction. Integrals over velocity space are evaluated following Gaussian quadrature rules. Linear terms are evolved implicitly in time, while nonlinear terms are evolved explicitly by a third-order Adams-Bashforth method. Collisions are treated using a fully conservative, linearized,

and gyroaveraged collision operator [72, 73].

5.2. Antenna Parameter Determination

Incompressible MHD turbulence is mediated by counterpropagating Alfvén waves since only counterpropagating waves interact nonlinearly [4, 5, 7, 8, 10]. If one adopts the convention that $\omega > 0$, then counterpropagating waves are described by oppositely signed parallel wave numbers. Also, for the nonlinearity to be nonzero, the polarization in the perpendicular plane of the counterpropagating Alfvén waves cannot be coplanar [10]. Note that these properties make Alfvénic turbulence inherently three dimensional [46, 12, 10]. We initialize counterpropagating and perpendicularly polarized Alfvén waves in our simulation by driving the four lowest wavenumber modes in our domain. If the modes are labelled $(k_x L_\perp, k_y L_\perp, k_z L_\parallel)$, where the simulation domain is $2\pi(L_\perp, L_\perp, L_\parallel)$, the driven Fourier modes are $(1, 0, \pm 1)$ and $(0, 1, \pm 1)$. Note that the amplitude of each driven mode can be independently specified. By specifying more energy in the field parallel or anti-parallel antenna components, imbalanced turbulence can be generated.

An arbitrary number of modes may be driven in AstroGK, however, we find that driving just these four modes is sufficient to develop a state of strong Alfvénic turbulence. Driving only at the smallest wave numbers in the domain is consistent with the physical model that the largest scales in our simulation receive energy through nonlinear interactions between counterpropagating Alfvén waves at scales slightly larger than the simulation domain.

The condition of critical balance [8] is used to determine the appropriate driving amplitude for the antenna to ensure that a state of strong turbulence is achieved in the simulation. The importance of specifying an amplitude sufficient to achieve strong turbulence cannot be underestimated—many existing plasma turbulence simulations in the literature do not specify sufficiently large driving amplitudes (or initial amplitudes for the case of decaying turbulence simulations), and consequently only a state of weak turbulence is achieved. Critical balance can be expressed as a balance between the linear frequency $\omega_l = k_z v_A$ and the nonlinear frequency, $\omega_l \sim \omega_{nl} = C_2 k_\perp v_\perp$ [14, 74], where C_2 is an order unity Kolmogorov constant. The MHD Alfvén wave linear eigenfunction satisfies $v_\perp = \pm \delta B_\perp / \sqrt{4\pi n_{0i} m_i}$. At $k_\perp \rho_i \gtrsim 1$, the Alfvén wave transitions into the dispersive kinetic Alfvén wave (KAW). More generally, the linear eigenfunction of the Alfvén/KAW satisfies $v_\perp = \bar{\omega}_l \delta B_\perp / \sqrt{4\pi n_{0i} m_i}$ [14], where

$$\bar{\omega}_l = \frac{\omega_l}{k_\parallel v_A} = \pm \sqrt{1 + \frac{(k_\perp \rho_i)^2}{\beta_i + 2/(1 + T_e/T_i)}} \quad (18)$$

is the linear dispersion relation of Alfvén/KAWs and $\beta_i = v_{ti}^2/v_A^2$. Using the eigenfunction relationship and (8), we can express critical balance in terms of \tilde{A}_z , $\omega_l \sim C_2 k_\perp^2 \bar{\omega}_l \tilde{A}_z / \sqrt{4\pi n_{0i} m_i}$, where \tilde{A}_z is the Fourier coefficient of the parallel vector potential. Therefore, driving critically balance turbulence at a given scale

requires that the steady-state antenna amplitude satisfy

$$\tilde{A}_z = \frac{\omega_l \sqrt{4\pi n_{0i} m_i}}{k_\perp^2 C_2 \bar{\omega}_l}. \quad (19)$$

As noted in section 4, the long-time response of the antenna is a Lorentzian. In the presence of a plasma, the long-time energy response in a particular wavenumber interval of the plasma remains Lorentzian and takes the form

$$|A_z(t \rightarrow \infty)|^2 = \frac{N A_0^2}{(\bar{\omega} - \bar{\omega}_0)^2 + (\bar{\gamma}_l + \bar{\gamma}_{nl})^2}, \quad (20)$$

where N is the number of modes driven, overbar indicates normalization by $k_\parallel v_A$, ω_0 is the antenna frequency, γ_l is the linear damping rate, and $\gamma_{nl} \simeq \omega_{nl}$ is the nonlinear energy transfer rate of energy out of the driven wave mode. Since we typically drive at $k_\perp \rho_i \lesssim 1$, the linear damping rate will be much smaller than the nonlinear energy transfer rate: $\gamma_l \ll \omega_{nl}$. Also, $\omega_l \sim \omega_{nl}$ in critical balance. Due to the shifting frequency of the antenna, $\bar{\omega} - \bar{\omega}_0 \sim [0, 1] \bar{\omega}_{nl} \sim [0, 1] \bar{\omega}_l$. To account for this, we introduce a parameter $\delta \in [1, 2]$ so that the denominator becomes $\bar{\omega}_l^2 \delta$. Therefore,

$$|A_z(t \rightarrow \infty)| = \frac{\sqrt{N} A_0}{\bar{\omega}_l \sqrt{\delta}}. \quad (21)$$

Equating (19) and (21), we arrive at the final form for the necessary driving amplitude to achieve a state of critically balanced, strong turbulence

$$A_0 = \frac{\bar{\omega}_l B_0 k_\parallel \sqrt{\delta}}{C_2 k_\perp^2 \sqrt{N}}. \quad (22)$$

We typically take $\delta = 2$ and $C_2 = 1$ to evaluate (22).

Finally, we need to specify the driving frequency, ω_0 , and decorrelation rate, γ_0 of the antenna. Since the energy entering our simulation is meant to mimic turbulence cascaded from larger scales, the frequency of the input energy should be lower than the linear frequency of the driven mode. Thus, we choose a driving frequency slightly below the characteristic linear frequency of the plasma at the driving wavelength, $\omega_l = k_\parallel v_A \bar{\omega}_l$. We typically take $\omega_0 = 0.9\omega_l$. We also want a decorrelation rate of order the linear frequency but below the antenna frequency since the nonlinear cascade rate at a given scale is expected to be equal to or less than the linear frequency at that scale. Therefore, $\gamma_0 \leq \omega_0$ based upon physical expectations, and we typically choose $\gamma_0 = -0.8\omega_l$.

Although we have focused here on a discussion of driving strong turbulence in our domain, by reducing the driving amplitude A_0 to a value less than that given by (22), we can intentionally drive weak turbulence. Perez and Boldyrev [51] noted that an elongated simulation domain is necessary for the optimal study of weak turbulence, which allows them to use reduced MHD simulations. Reduced MHD is indeed a limit of gyrokinetics [16]. As part of its ordering, gyrokinetics necessitates the use of an elongated simulation domain, which implies that the assumed ordering underlying our simulations can also be used for studying weak turbulence.

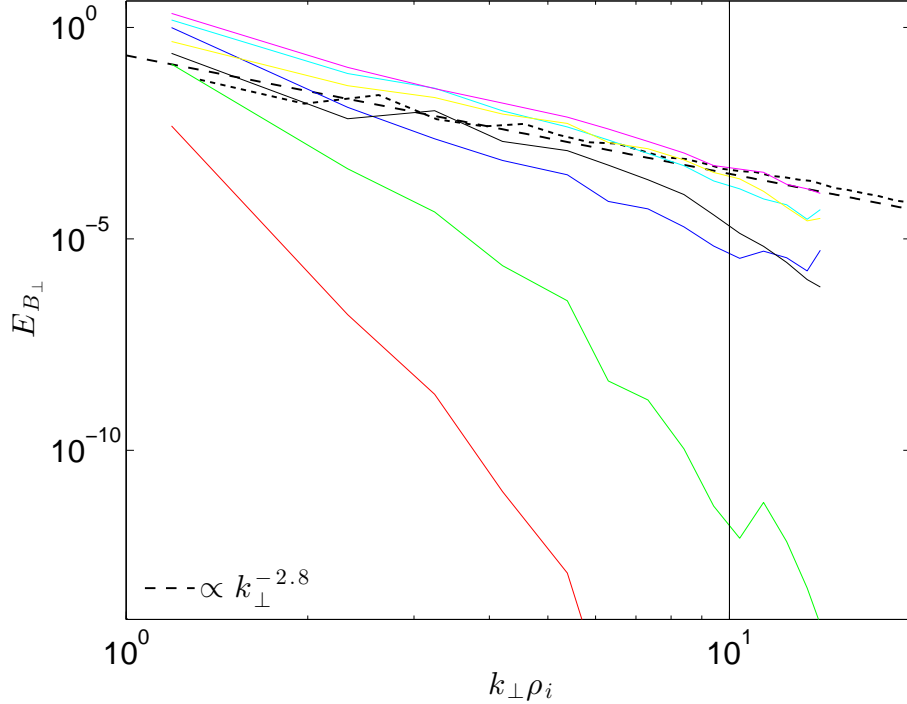


Figure 8: Evolution of the perpendicular magnetic energy spectrum for a $\beta_i = 1$ fully nonlinear AstroGK simulation driven as outlined in section 5.2. The solid lines represent the energy at $t \simeq 0.1, 0.2, 0.4, 0.8, 1.6, 3.2,$ and $6.4\tau_D$ (red, green, blue, cyan, magenta, yellow, and black respectively) and the dotted line is from a larger, higher resolution simulation with similar plasma parameters. The vertical line at $k_{\perp}\rho_i = 10$ represents the edge of the simulation domain.

5.3. Saturation of Strong Turbulence in AstroGK Simulations

Driving in the manner described above generates well-developed turbulence across the full simulation domain within approximately one domain-scale turnaround time: $\tau_D = 2\pi/\omega_D$. Since we choose to drive in critical balance, $\tau_D = \tau_{Alfven} = 2\pi/v_A k_{zD}$, where $k_{zD} = 2\pi/L_z$. To demonstrate this, we plot in Figure 8 the evolution of the perpendicular magnetic energy spectrum, $E_{B_{\perp}} = \delta B_{\perp}^2/k_{\perp}$, spanning 0.1 to $6.4\tau_D$ for a simulation of strong Alfvénic turbulence in a $\beta_i = 1$ plasma using AstroGK driven by the oscillating Langevin antenna as described above—full details of the simulation are provided in [50]. The specific parameters of the antenna for this simulation are: $\omega_0 = 1.14k_{zD}v_A \simeq \omega_l$, $\gamma_0 = -0.9k_{zD}v_A$, $A_0 = \rho_i B_0/\xi$, and with four driven wavenumber modes $(k_x, k_y, k_z/\xi)\rho_i = (1, 0, \pm 1)$ and $(0, 1, \pm 1)$, where the spatial extent of the domain is $(L_x, L_y, L_z) = 2\pi\rho_i(1, 1, 1/\xi)$ and ξ is an elongation factor. The time step at the beginning of the simulation was $\Delta t = 5 \times 10^{-3}/k_{zD}v_A$ but decreased to $\Delta t \simeq 2 \times 10^{-5}/k_{zD}v_A$ during the course of the simulation to ensure the Courant-Friedrichs-Lewy (CFL) condition is satisfied at the smallest spatial

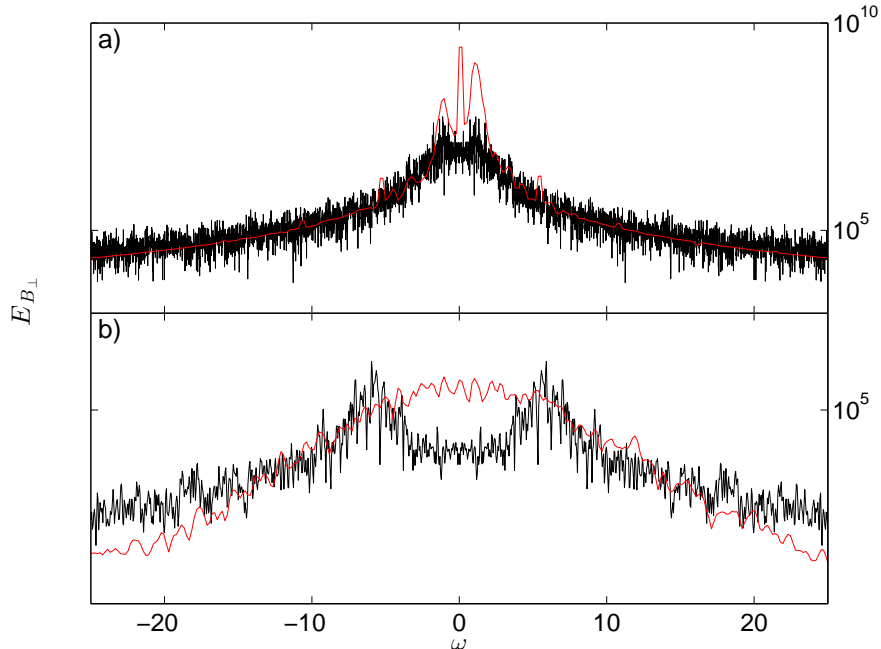


Figure 9: Plasma response to the oscillating Langevin antenna. In both panels, the plasma response is plotted in red and the antenna is black. Panel a) is the response for the driven mode with $k_{\perp}\rho_i = 1$ and $k_z\rho_i/\xi = 1$. The antenna parameters are the same as used in the simulation, $\omega_0 = \pm 1.14$ and $\gamma_0 = -0.9$. Panel b) is the response in the middle of the domain with $k_{\perp}\rho_i = 5$ and $k_z\rho_i/\xi = 1$. The antenna parameters are $\omega_0 = \pm 6$ and $\gamma_0 = -\omega_0/2\pi$.

scales. The only energy input into the system is via the oscillating Langevin antenna. Within one turnaround time, the spectrum develops an approximate $k_{\perp}^{-2.8}$ scaling, consistent with solar wind observations [25, 26, 28].

In addition, we plot the magnetic energy spectrum from a previously published AstroGK simulation over the entire dissipation range from the ion to the electron Larmor radius scale [46]. This simulation employs the same plasma parameters as employed above, but covers a much larger spatial dynamic range. The antenna and plasma parameters of the larger simulation are identical to the smaller simulation with the following exceptions: six modes were driven, $(k_x, k_y, k_z/\xi)\rho_i = (\pm 1, 0, \pm 1)$ and $(0, 1, \pm 1)$, and the ending time step was $\Delta t \simeq 2.4 \times 10^{-6}/k_z D v_A$. We see that the results of this larger simulation (dotted) agree well with the results of the smaller simulation in Figure 8.

5.4. Comparing Turbulent Driving to Fluctuations in Turbulence Simulations

In Figure 9, we examine the plasma response to the oscillating Langevin antenna for the same small simulation discussed above. In both panels, the red line is the plasma response, and the black line is the sum of antennae with positive and negative frequencies to represent waves driven up and down the

magnetic field. Both quantities have applied to them a boxcar average with a width of 2. In panel a) of the figure is the driven mode of the plasma with $k_{\perp}\rho_i = 1$ and $k_z\rho_i/\xi = 1$, and the antenna has the same parameters as those used in the simulation, $\omega_0 = \pm 1.14k_zDv_A$ and $\gamma_0 = -0.9k_zDv_A$. The linear frequency of this plasma mode is $\omega_l = 1.14k_zDv_A$, which corresponds to the driving frequency. Clearly, the plasma response of this mode is dominated by the driving. It can also be seen that more energy is driven into the positive frequency mode, which implies somewhat imbalanced driving. The accumulation of energy in the $\omega = 0$ mode is expected because this mode is responsible for nonlinear scattering in three-wave interactions of turbulence and is self-consistently generated [75, 7, 76, 50, 10].

In panel b) of Figure 9 is the plasma response in the middle of the perpendicular domain, $k_{\perp}\rho_i = 5$ and $k_z\rho_i/\xi = 1$. The simulation is not driven at this wavenumber, but it is valuable to compare the natural plasma response to that of the oscillating Langevin antenna to determine if the antenna does indeed resemble turbulence at a given scale. The linear frequency associated with this mode is $\omega \simeq 6$, so we model the plasma response with an antenna having a frequency $\omega_0 = 6$. We choose an antenna decorrelation rate $\gamma_0 = -\omega_0/2\pi$ to fit the response. Although the antenna fit to the plasma appears poor, the subjective appearance is deceptive. The discussion in §3 suggests the plasma will respond poorly to energy input above the linear frequency of a given mode. Therefore, the apparent excess energy in the tails of the antenna will couple poorly to the plasma. Further, the valley between the antenna peaks will be self-consistently populated by low frequency modes generated in critically balanced turbulence [10].

6. Comparison to Other Driving Methods

We have described one method by which turbulence simulations can be driven; however, many methods are used throughout the literature to initialize or drive turbulence. We now briefly discuss the two most common approaches to generating plasma turbulence in numerical simulations.

6.1. Decaying

One common method to inject energy into turbulence simulations is to initialize a set of modes at the beginning of the simulation and observe how they decay and energy is cascaded to smaller scales over time. Decaying simulations of turbulence can be initialized in a variety of ways to facilitate the study of various phenomena, for example: generalized Orszag-Tang vortices to simulate magnetic reconnection driven turbulence in electron MHD (EMHD) [77] or hybrid simulations [17], a spectrum of energy across a band of Fourier modes with varying angular distributions in EMHD [78], exact plasma eigenmodes with equal energy in particle-in-cell simulations [58, 79], energy in only the largest Fourier mode in gyrokinetic simulations [80], equal energy across a collection of large scale Fourier modes in Landau fluid simulations [81].

Decaying turbulence simulations have the advantage of specifying an exact initial condition and energy state, which provide precise control of the simulation. This is ideal when the goal of the simulation is to either study the evolution of exact plasma eigenmodes or a specific physical configuration (e.g., Orszag-Tang vortices); however, it is unlikely to represent many physical systems since a collection of isolated exact eigenmodes or an ideal spatial configuration are rare events. Therefore, decaying simulations tend to represent highly idealized physical processes. Also, decaying simulations are incapable of achieving a steady-state by definition.

6.2. Direct Injection of Noise

Direct injection of noise has been used to drive many turbulence simulations. The simulations employ a variety of methods for injecting energy; however, they all do so by setting the Fourier coefficients of the velocity and/or magnetic field to random numbers at either each time step or over finitely correlated times for a band of wave vectors with appropriate normalizations and constraints, e.g., $\nabla \cdot \mathbf{B} = 0$, applied to the Fourier coefficients prior to advancing the fields. The Fourier coefficients are typically updated by randomizing only the phase with fixed amplitude integrated over all driven wavenumbers [37, 51, 65, 49], randomizing the phase and amplitude within a Gaussian envelope [38], or choosing random phase, amplitude, and driving wavenumber from a band of wavenumbers [82]. Müller and Grappin [83] drive a simulation by initializing and "freezing" modes in a given band of wavenumbers, which is similar to the method used in decaying turbulence simulations except that the initial condition is held fixed.

As demonstrated by its ubiquity, this method of driving is capable of generating strong turbulence; however, the physical motivation for the various driving methods outlined above is unlikely to be representative of large scale energy being cascaded into the simulation domain. Although useful from an analysis standpoint, injecting energy with fixed amplitude and constant or varying phase with respect to time is not well motivated physically. Randomizing the phase and amplitude from a range of Gaussian distributed amplitudes is likely more realistic, but still leaves unspecified the frequency spectrum of the energy input into the system.

Many simulations employ finite time correlated driving wherein the Fourier coefficients are updated at some fraction of the system crossing time. For this type of driving, the frequency of the energy input is difficult to determine without greater detail than is typically provided. However, simulations that employ a delta-correlated driving correspond to directly injecting white noise in frequency. White noise driving can be described by an equation similar to equation (15) in the absence of oscillations and damping,

$$\frac{da}{dt} = \sqrt{2}A_0u_n. \quad (23)$$

The evolution of this type of antenna is depicted in Figure 10. The ensemble average of 64 similar runs for driving of this type is $\langle |a| \rangle = 108.1649 \pm$

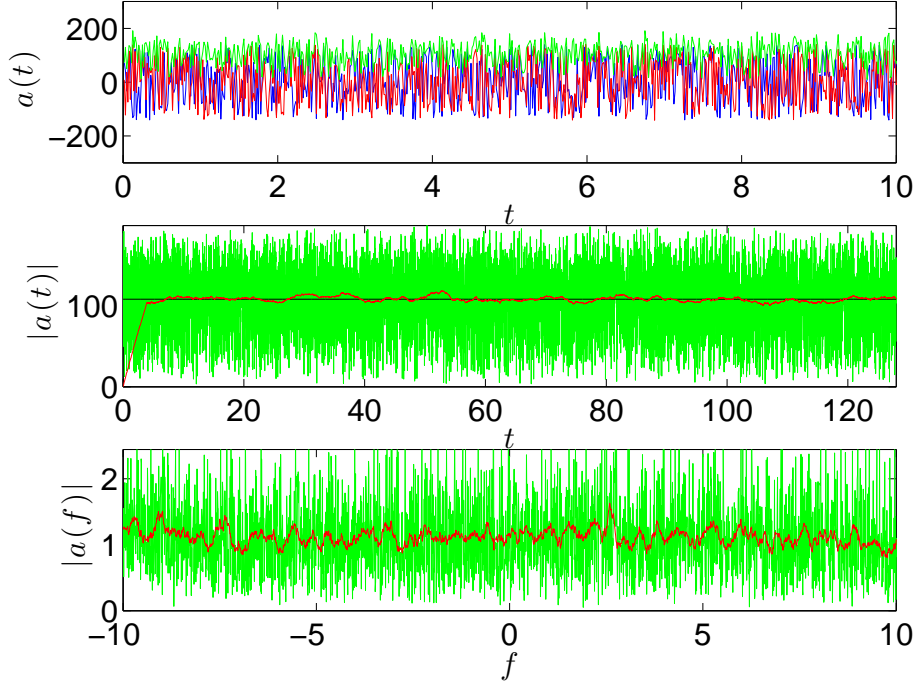


Figure 10: Temporal evolution of a single, delta-correlated white noise antenna with $A_0 = 100$. Top: Real (blue), imaginary (red), and the magnitude (green) of the complex vector potential over 10 periods. Middle: Magnitude (green), boxcar average of the magnitude (red), and overall average of the magnitude (black) of a over 128 periods. Bottom: The frequency spectrum of the antenna (green) and its boxcar average (red).

40.28515. As expected, the energy injected by white noise is evenly distributed across all frequencies. This will result in a magnetic energy spectrum $E(\omega) \propto \delta B^2/\omega \propto \omega^{-1}$.

White noise driving might be motivated by an attempt to mimic the energy containing region of turbulence since the energy containing region is expected to be inhomogeneous and have an energy spectrum that scales as k^{-1} . Although the spectral exponent is -1 , this is due to a constant energy distribution in space. The temporal distribution of energy in this region is not known but is unlikely to be constant. Note that solar wind observations of this region depict a frequency spectrum with spectral exponent -1 ; however, this is a measurement of spatial plasma fluctuations and not temporal plasma oscillations due to the high Mach number flows and single point measurements of the solar wind, e.g., see [3].

Most of the methods outlined in this section reach a steady-state within a few turnaround times, so they are efficient at developing strong turbulence. Despite the rapidity with which they develop strong turbulence, the methods tend to pollute wavenumbers approximately a factor of two or more beyond

their driven range with driving effects. For instance, Perez and Boldyrev [51] drive in the perpendicular direction with $1 \leq k_{\perp} \leq 2$, but the driving can be seen to affect perpendicular wavenumbers up to $k_{\perp} \lesssim 4$.

7. Summary

We have presented a novel method for driving plasma turbulence simulations via an oscillating Langevin antenna that is evolved via the Langevin equation. This method of driving plasma turbulence was motivated by a desire to perform turbulence simulations in which the largest scale of the simulation is smaller than the scale at which energy is physically injected into the plasma environment that is being modeled. In other words, the outer scale of the inertial range of the physical turbulent system is larger than the simulation domain scale. An overview of the properties of plasma turbulence relevant to driving in a physical manner were explored in §2. Also, the response of the plasma to simple sinusoidal driving was considered in §3, where we found that the driving frequency of the antenna must be below the characteristic linear frequency of the plasma to avoid an impedance mismatch.

Driving turbulence via the oscillating Langevin antenna requires counter-propagating Alfvén waves, in which each driven plane Alfvén wave is completely characterized by four parameters: the wavevector \mathbf{k} , amplitude A_0 , frequency ω_0 , and decorrelation rate γ_0 . We have shown that the oscillating Langevin antenna represents an efficient and flexible method to drive Alfvénic turbulence simulations that mimics cascaded turbulent energy entering a numerical simulation domain from scales larger than those included in the simulation. By varying the antenna amplitude, we are able to drive strong or weak turbulence into the simulation domain, and the turbulence can be balanced or imbalanced.

The domain of validity of the antenna was explored in §4, where we found that the antenna is well behaved for de-correlation rates $|\gamma_0| \lesssim 4\omega_0$ and time steps $\Delta t \lesssim 0.4/\omega_0$. For all cases of interest, the nonlinear cascade rate is less than or equal to the linear frequency, so $|\gamma_0| \lesssim 4\omega_0$ is always satisfied. Also, $\Delta t \ll 1/\omega_l$ to ensure numerical accuracy of any simulation, where ω_l is the linear response of the plasma. Therefore, the antenna is expected to be well behaved in any reasonable turbulence simulation.

In §6, we examined two of the most common methods, decaying and injection of noise, of generating turbulence in numerical simulations and compared them to the oscillating Langevin antenna. We found that both of these common methods have certain inherent advantages but that neither is well motivated physically nor does either method represent a realistic frequency response of energy entering the simulation domain.

Although our presentation of the oscillating Langevin antenna has focused on its usage to drive Alfvénic turbulence in the Astrophysical Gyrokinetics Code, the prescription for the antenna given in §4 is sufficiently generic to permit implementation of similar schemes in other numerical simulations of plasma turbulence.

Acknowledgements

Support was provided by NSF CAREER Award AGS-1054061 and NSF grant PHY-10033446.

References

- [1] J. W. Belcher, L. Davis, Large-Amplitude Alfvén Waves in the Interplanetary Medium, 2, *J. Geophys. Res.* 76 (1971) 3534–3563.
- [2] C.-Y. Tu, E. Marsch, MHD structures, waves and turbulence in the solar wind: Observations and theories, *Space Science Reviews* 73 (1995) 1–2.
- [3] R. Bruno, V. Carbone, The Solar Wind as a Turbulence Laboratory, *Living Reviews in Solar Physics* 2 (4).
- [4] R. S. Iroshnikov, The turbulence of a conducting fluid in a strong magnetic field, *Astron. Zh.* 40 (1963) 742, English Translation: *Sov. Astron.*, 7 566 (1964).
- [5] R. H. Kraichnan, Inertial Range Spectrum of Hydromagnetic Turbulence, *Phys. Fluids* 8 (1965) 1385–1387.
- [6] J. V. Shebalin, W. H. Matthaeus, D. Montgomery, Anisotropy in MHD turbulence due to a mean magnetic field, *J. Plasma Phys.* 29 (1983) 525–547.
- [7] S. Sridhar, P. Goldreich, Toward a Theory of Interstellar Turbulence I. Weak Alfvénic Turbulence, *Astrophys. J.* 433 (1994) 612–621.
- [8] P. Goldreich, S. Sridhar, Toward a Theory of Interstellar Turbulence II. Strong Alfvénic Turbulence, *Astrophys. J.* 438 (1995) 763–775.
- [9] S. Boldyrev, Spectrum of Magnetohydrodynamic Turbulence, *Phys. Rev. Lett.* 96 (11) (2006) 115002–+, doi:10.1103/PhysRevLett.96.115002.
- [10] G. G. Howes, K. D. Nielson, Alfvén Wave Collisions, The Fundamental Building Block of Plasma Turbulence I: Asymptotic Solution, *Phys. Plasmas* 20 (2013) 072302.
- [11] G. I. Taylor, The Spectrum of Turbulence, *Proc. Roy. Soc. A* 164 (1938) 476–490.
- [12] G. G. Howes, D. J. Drake, K. D. Nielson, T. A. Carter, C. A. Kletzing, F. Skiff, Toward Astrophysical Turbulence in the Laboratory, *Phys. Rev. Lett.* 109 (25) 255001, doi:10.1103/PhysRevLett.109.255001.
- [13] W. Gekelman, Review of laboratory experiments on Alfvén waves and their relationship to space observations, *J. Geophys. Res.* 104 (1999) 14417–14436, doi:10.1029/98JA00161.

- [14] G. G. Howes, S. C. Cowley, W. Dorland, G. W. Hammett, E. Quataert, A. A. Schekochihin, A model of turbulence in magnetized plasmas: Implications for the dissipation range in the solar wind, *J. Geophys. Res.* 113 (2008) A05103, doi:10.1029/2007JA012665.
- [15] G. G. Howes, Inertial range turbulence in kinetic plasmas, *Phys. Plasmas* 15 (5) (2008) 055904, doi:10.1063/1.2889005.
- [16] A. A. Schekochihin, S. C. Cowley, W. Dorland, G. W. Hammett, G. G. Howes, E. Quataert, T. Tatsuno, Astrophysical Gyrokinetics: Kinetic and Fluid Turbulent Cascades in Magnetized Weakly Collisional Plasmas, *Astrophys. J. Supp.* 182 (2009) 310–377, doi:10.1088/0067-0049/182/1/310.
- [17] T. N. Parashar, M. A. Shay, P. A. Cassak, W. H. Matthaeus, Kinetic dissipation and anisotropic heating in a turbulent collisionless plasma, *Phys. Plasmas* 16 (3) (2009) 032310–+, doi:10.1063/1.3094062.
- [18] K. T. Osman, W. H. Matthaeus, A. Greco, S. Servidio, Evidence for Inhomogeneous Heating in the Solar Wind, *Astrophys. J. Lett.* 727 L11, doi:10.1088/2041-8205/727/1/L11.
- [19] S. Servidio, F. Valentini, F. Califano, P. Veltri, Local Kinetic Effects in Two-Dimensional Plasma Turbulence, *Phys. Rev. Lett.* 108 (4) 045001, doi:10.1103/PhysRevLett.108.045001.
- [20] J. M. TenBarge, G. G. Howes, Current Sheets and Collisionless Dissipation in Kinetic Plasma Turbulence, *Astrophys. J. Lett.* 771 (2013) L27.
- [21] H. Karimabadi, V. Roytershteyn, M. Wan, W. H. Matthaeus, W. Daughton, P. Wu, M. Shay, B. Loring, J. Borovsky, E. Leonardis, S. C. Chapman, T. K. M. Nakamura, Coherent structures, intermittent turbulence, and dissipation in high-temperature plasmas, *Phys. Plasmas* 20 (1) (2013) 012303, doi:10.1063/1.4773205.
- [22] P. J. Coleman, Jr., Turbulence, Viscosity, and Dissipation in the Solar-Wind Plasma, *Astrophys. J.* 153 (1968) 371–388.
- [23] R. J. Leamon, C. W. Smith, N. F. Ness, W. H. Matthaeus, H. K. Wong, Observational Constraints on the Dynamics of the Interplanetary Magnetic Field Dissipation Range, *J. Geophys. Res.* 103 (1998) 4775–4787.
- [24] F. Sahraoui, M. L. Goldstein, P. Robert, Y. V. Khotyaintsev, Evidence of a Cascade and Dissipation of Solar-Wind Turbulence at the Electron Gyroscale, *Physical Review Letters* 102 (23) (2009) 231102–+, doi:10.1103/PhysRevLett.102.231102.
- [25] K. H. Kiyani, S. C. Chapman, Y. V. Khotyaintsev, M. W. Dunlop, F. Sahraoui, Global scale-invariant dissipation in collisionless plasma turbulence, *Physical Review Letters* 103 (2009) 075006.

- [26] O. Alexandrova, J. Saur, C. Lacombe, A. Mangeney, J. Mitchell, S. J. Schwartz, P. Robert, Universality of Solar-Wind Turbulent Spectrum from MHD to Electron Scales, *Phys. Rev. Lett.* 103 (16) (2009) 165003–+, doi: 10.1103/PhysRevLett.103.165003.
- [27] C. H. K. Chen, T. S. Horbury, A. A. Schekochihin, R. T. Wicks, O. Alexandrova, J. Mitchell, Anisotropy of Solar Wind Turbulence between Ion and Electron Scales, *Phys. Rev. Lett.* 104 (25) (2010) 255002–+, doi: 10.1103/PhysRevLett.104.255002.
- [28] F. Sahraoui, M. L. Goldstein, G. Belmont, P. Canu, L. Rezeau, Three Dimensional Anisotropic k Spectra of Turbulence at Subproton Scales in the Solar Wind, *Phys. Rev. Lett.* 105 (13) (2010) 131101–+, doi: 10.1103/PhysRevLett.105.131101.
- [29] O. Alexandrova, C. Lacombe, A. Mangeney, R. Grappin, M. Maksimovic, Solar Wind Turbulent Spectrum at Plasma Kinetic Scales, *Astrophys. J.* 760 121, doi:10.1088/0004-637X/760/2/121.
- [30] R. T. Wicks, A. Mallet, T. S. Horbury, C. H. K. Chen, A. A. Schekochihin, J. J. Mitchell, Alignment and Scaling of Large-Scale Fluctuations in the Solar Wind, *Phys. Rev. Lett.* 110 (2) 025003, doi: 10.1103/PhysRevLett.110.025003.
- [31] T. S. Horbury, M. Forman, S. Oughton, Anisotropic Scaling of Magneto-hydrodynamic Turbulence, *Phys. Rev. Lett.* 101 (2008) 175005, doi: 10.1103/PhysRevLett.101.175005.
- [32] J. J. Podesta, Dependence of Solar-Wind Power Spectra on the Direction of the Local Mean Magnetic Field, *Astrophys. J.* 698 (2009) 986–999, doi: 10.1088/0004-637X/698/2/986.
- [33] R. T. Wicks, T. S. Horbury, C. H. K. Chen, A. A. Schekochihin, Power and spectral index anisotropy of the entire inertial range of turbulence in the fast solar wind, *Mon. Not. Roy. Astron. Soc.* 407 (2010) L31–L35, doi: 10.1111/j.1745-3933.2010.00898.x.
- [34] Q. Y. Luo, D. J. Wu, Observations of Anisotropic Scaling of Solar Wind Turbulence, *Astrophys. J. Lett.* 714 (2010) L138–L141, doi:10.1088/2041-8205/714/1/L138.
- [35] C. H. K. Chen, A. Mallet, A. A. Schekochihin, T. S. Horbury, R. T. Wicks, S. D. Bale, Three-Dimensional Structure of Solar Wind Turbulence, *ArXiv e-prints* .
- [36] Y. Narita, S. P. Gary, S. Saito, K.-H. Glassmeier, U. Motschmann, Dispersion relation analysis of solar wind turbulence, *Geophys. Res. Lett.* 38 (2011) L05101, doi:10.1029/2010GL046588.

- [37] J. Cho, E. T. Vishniac, The Anisotropy of Magnetohydrodynamic Alfvénic Turbulence, *Astrophys. J.* 539 (2000) 273–282.
- [38] J. Maron, P. Goldreich, Simulations of Incompressible Magnetohydrodynamic Turbulence, *Astrophys. J.* 554 (2001) 1175–1196.
- [39] J. Cho, A. Lazarian, Compressible Sub-Alfvénic MHD Turbulence in Low- β Plasmas, *Phys. Rev. Lett.* 88 (24) 245001, doi:10.1103/PhysRevLett.88.245001.
- [40] J. Mason, F. Cattaneo, S. Boldyrev, Dynamic Alignment in Driven Magnetohydrodynamic Turbulence, *Phys. Rev. Lett.* 97 (25) (2006) 255002–+, doi:10.1103/PhysRevLett.97.255002.
- [41] J. Mason, J. C. Perez, F. Cattaneo, S. Boldyrev, Extended Scaling Laws in Numerical Simulations of Magnetohydrodynamic Turbulence, *Astrophys. J. Lett.* 735 L26, doi:10.1088/2041-8205/735/2/L26.
- [42] J. C. Perez, J. Mason, S. Boldyrev, F. Cattaneo, On the Energy Spectrum of Strong Magnetohydrodynamic Turbulence, *Phys. Rev. X* 2 (4) 041005, doi:10.1103/PhysRevX.2.041005.
- [43] G. G. Howes, W. Dorland, S. C. Cowley, G. W. Hammett, E. Quataert, A. A. Schekochihin, T. Tatsuno, Kinetic Simulations of Magnetized Turbulence in Astrophysical Plasmas, *Phys. Rev. Lett.* 100 (6) (2008) 065004, doi:10.1103/PhysRevLett.100.065004.
- [44] C. S. Salem, G. G. Howes, D. Sundkvist, S. D. Bale, C. C. Chaston, C. H. K. Chen, F. S. Mozer, Identification of Kinetic Alfvén Wave Turbulence in the Solar Wind, *Astrophys. J. Lett.* 745 L9, doi:10.1088/2041-8205/745/1/L9.
- [45] J. M. TenBarge, J. J. Podesta, K. G. Klein, G. G. Howes, Interpreting Magnetic Variance Anisotropy Measurements in the Solar Wind, *Astrophys. J.* 753 107, doi:10.1088/0004-637X/753/2/107.
- [46] G. G. Howes, J. M. TenBarge, W. Dorland, E. Quataert, A. A. Schekochihin, R. Numata, T. Tatsuno, Gyrokinetic Simulations of Solar Wind Turbulence from Ion to Electron Scales, *Phys. Rev. Lett.* 107 (3) (2011) 035004–+, doi:10.1103/PhysRevLett.107.035004.
- [47] J. M. TenBarge, G. G. Howes, W. Dorland, Collisionless Dissipation at Electron Scales in the Solar Wind, *Astrophys. J.* 774 (2013) 107, submitted.
- [48] J. Cho, A. Lazarian, The Anisotropy of Electron Magnetohydrodynamic Turbulence, *Astrophys. J. Lett.* 615 (2004) L41–L44, doi:10.1086/425215.
- [49] J. Cho, A. Lazarian, Simulations of Electron Magnetohydrodynamic Turbulence, *Astrophys. J.* 701 (2009) 236–252, doi:10.1088/0004-637X/701/1/236.

- [50] J. M. TenBarge, G. G. Howes, Evidence of Critical Balance in Kinetic Alfvén Wave Turbulence Simulations, *Phys. Plasmas* 19 (5) (2012) 055901.
- [51] J. C. Perez, S. Boldyrev, On Weak and Strong Magnetohydrodynamic Turbulence, *Astrophys. J. Lett.* 672 (2008) L61–L64, doi:10.1086/526342.
- [52] J. C. Perez, S. Boldyrev, Strong magnetohydrodynamic turbulence with cross helicity, *Physics of Plasmas* 17 (5) (2010) 055903, doi:10.1063/1.3396370.
- [53] S. P. Gary, S. Saito, Y. Narita, Whistler Turbulence Wavevector Anisotropies: Particle-in-cell Simulations, *Astrophys. J.* 716 (2010) 1332–1335, doi:10.1088/0004-637X/716/2/1332.
- [54] S. A. Markovskii, B. J. Vasquez, A Short-timescale Channel of Dissipation of the Strong Solar Wind Turbulence, *Astrophys. J.* 739 22, doi:10.1088/0004-637X/739/1/22.
- [55] B. J. Vasquez, S. A. Markovskii, Velocity Power Spectra from Cross-field Turbulence in the Proton Kinetic Regime, *Astrophys. J.* 747 19, doi:10.1088/0004-637X/747/1/19.
- [56] S. Donato, S. Servidio, P. Dmitruk, V. Carbone, M. A. Shay, P. A. Cassak, W. H. Matthaeus, Reconnection events in two-dimensional Hall magnetohydrodynamic turbulence, *Phys. Plasmas* 19 (9) (2012) 092307, doi:10.1063/1.4754151.
- [57] M. Wan, W. H. Matthaeus, H. Karimabadi, V. Roytershteyn, M. Shay, P. Wu, W. Daughton, B. Loring, S. C. Chapman, Intermittent Dissipation at Kinetic Scales in Collisionless Plasma Turbulence, *Phys. Rev. Lett.* 109 (19) 195001, doi:10.1103/PhysRevLett.109.195001.
- [58] S. Saito, S. P. Gary, H. Li, Y. Narita, Whistler turbulence: Particle-in-cell simulations, *Phys. Plasmas* 15 (10) (2008) 102305–+, doi:10.1063/1.2997339.
- [59] R. Numata, G. G. Howes, T. Tatsuno, M. Barnes, W. Dorland, AstroGK: Astrophysical Gyrokinetics Code, *J. Comp. Phys.* 229 (2010) 9347–9372, doi:10.1016/j.jcp.2010.09.006.
- [60] S. Saito, S. P. Gary, Y. Narita, Wavenumber spectrum of whistler turbulence: Particle-in-cell simulation, *Phys. Plasmas* 17 (12) (2010) 122316–+, doi:10.1063/1.3526602.
- [61] T. N. Parashar, S. Servidio, B. Breech, M. A. Shay, W. H. Matthaeus, Kinetic driven turbulence: Structure in space and time, *Phys. Plasmas* 17 (10) (2010) 102304, doi:10.1063/1.3486537.
- [62] O. Chang, S. Peter Gary, J. Wang, Whistler turbulence forward cascade: Three-dimensional particle-in-cell simulations, *Geophys. Res. Lett.* 38 L22102, doi:10.1029/2011GL049827.

- [63] S. P. Gary, O. Chang, J. Wang, Forward Cascade of Whistler Turbulence: Three-dimensional Particle-in-cell Simulations, *Astrophys. J.* 755 142, doi:10.1088/0004-637X/755/2/142.
- [64] J. C. Higdon, Density Fluctuations in the Interstellar Medium: Evidence for Anisotropic Magnetogasdynamic Turbulence I. Model and Astrophysical Sites, *Astrophys. J.* 285 (1984) 109–123.
- [65] A. Beresnyak, A. Lazarian, Comparison of Spectral Slopes of Magneto-hydrodynamic and Hydrodynamic Turbulence and Measurements of Alignment Effects, *Astrophys. J.* 702 (2009) 1190–1198, doi:10.1088/0004-637X/702/2/1190.
- [66] W. M. Elsasser, The Hydromagnetic Equations, *Physical Review* 79 (1950) 183–183, doi:10.1103/PhysRev.79.183.
- [67] T. N. Parashar, S. Servidio, M. A. Shay, B. Breech, W. H. Matthaeus, Effect of driving frequency on excitation of turbulence in a kinetic plasma, *Phys. Plasmas* 18 (9) (2011) 092302–+, doi:10.1063/1.3630926.
- [68] D. S. Lemons, *An Introduction to Stochastic Processes in Physics*, Baltimore: Johns Hopkins University Press, 2002.
- [69] P. Langevin, On the Theory of Brownian Motion, *C. R. Acad. Sci. (Paris)* 146 (1908) 530–533.
- [70] E. A. Frieman, L. Chen, Nonlinear gyrokinetic equations for low-frequency electromagnetic waves in general plasma equilibria, *Phys. Fluids* 25 (1982) 502–508.
- [71] G. G. Howes, S. C. Cowley, W. Dorland, G. W. Hammett, E. Quataert, A. A. Schekochihin, Astrophysical Gyrokinetics: Basic Equations and Linear Theory, *Astrophys. J.* 651 (2006) 590–614, doi:10.1086/506172.
- [72] I. G. Abel, M. Barnes, S. C. Cowley, W. Dorland, A. A. Schekochihin, Linearized model Fokker-Planck collision operators for gyrokinetic simulations. I. Theory, *Phys. Plasmas* 15 (12) (2008) 122509–+, doi:10.1063/1.3046067.
- [73] M. Barnes, I. G. Abel, W. Dorland, D. R. Ernst, G. W. Hammett, P. Ricci, B. N. Rogers, A. A. Schekochihin, T. Tatsuno, Linearized model Fokker-Planck collision operators for gyrokinetic simulations. II. Numerical implementation and tests, *Phys. Plasmas* 16 (7) (2009) 072107–+, doi:10.1063/1.3155085.
- [74] G. G. Howes, J. M. TenBarge, W. Dorland, A weakened cascade model for turbulence in astrophysical plasmas, *Phys. Plasmas* 18 (10) (2011) 102305, doi:10.1063/1.3646400.
- [75] D. Montgomery, L. Turner, Anisotropic Magnetohydrodynamic Turbulence in a Strong External Magnetic Field, *Phys. Fluids* 24 (1981) 825–831.

- [76] S. Galtier, A. Bhattacharjee, Anisotropic weak whistler wave turbulence in electron magnetohydrodynamics, *Phys. Plasmas* 10 (2003) 3065–3076, doi:10.1063/1.1584433.
- [77] D. Biskamp, E. Schwarz, A. Zeiler, A. Celani, J. F. Drake, Electron Magnetohydrodynamic Turbulence, *Phys. Plasmas* 6 (1999) 751–758.
- [78] S. Dastgeer, A. Das, P. Kaw, P. H. Diamond, Whistlerization and anisotropy in two-dimensional electron magnetohydrodynamic turbulence, *Phys. Plasmas* 7 (2000) 571–579, doi:10.1063/1.873843.
- [79] V. A. Svidzinski, H. Li, H. A. Rose, B. J. Albright, K. J. Bowers, Particle in cell simulations of fast magnetosonic wave turbulence in the ion cyclotron frequency range, *Phys. Plasmas* 16 (12) (2009) 122310–+, doi: 10.1063/1.3274559.
- [80] T. Tatsuno, M. Barnes, S. C. Cowley, W. Dorland, G. G. Howes, R. Numata, G. G. Plunk, A. A. Schekochihin, Gyrokinetic simulation of entropy cascade in two-dimensional electrostatic turbulence, *J. Plasma Fusion Res.* Accepted.
- [81] P. Hunana, D. Laveder, T. Passot, P. L. Sulem, D. Borgogno, Reduction of Compressibility and Parallel Transfer by Landau Damping in Turbulent Magnetized Plasmas, *Astrophys. J.* 743 128, doi:10.1088/0004-637X/743/2/128.
- [82] N. E. L. Haugen, A. Brandenburg, W. Dobler, Is Nonhelical Hydromagnetic Turbulence Peaked at Small Scales?, *Astrophys. J. Lett.* 597 (2003) L141–L144, doi:10.1086/380189.
- [83] W.-C. Müller, R. Grappin, Spectral Energy Dynamics in Magnetohydrodynamic Turbulence, *Phys. Rev. Lett.* 95 (11) 114502, doi: 10.1103/PhysRevLett.95.114502.